Strong Optical Excitation and High Thermoelectric Performance in 2D Holey-Phosphorene Monolayer

Nabil Khossossi, Deobrat Singh, Wei Luo, and Rajeev Ahuja*

Through density functional theory (DFT)-based computations, a systematic exploration of the newly predicted 2D phosphorene allotrope, namely holey-phosphorene (HP), is carried out. It is revealed that HP shows a semiconducting nature with an indirect bandgap of 0.83 eV upon Perdew-Burke-Ernzerhof (PBE) functional. Then, to survey the optical features, a (G_0W_0)-based approach is employed to solve the Bethe–Salpeter equation to derive the intra-layer excitonic effects. It is derived via the absorption spectrum, that HP presents an excitonic binding strength of 1.47/1.96 eV along the x/y-direction with the first peak of the absorption at 0.92/0.43 eV for the x/y-direction. The thermoelectric properties are also explored in detail and reveal a very high thermal power value along with an enhanced figure of merit (ZT) of about 3.6. The 2D HP monolayer for thermoelectric performance has high thermoelectric conversion efficiency (TCE) and is estimated to be about 22%. All these outstanding findings may be attributed to the quantum confinement effect of the porous geometry of the 2D HP nanosheet, thereby confirming its relevance as a prospect for high-performance optoelectronic and thermoelectric engineering systems.

1. Introduction

Driven by the successful exfoliation of a 2D graphene monolayer,[1] tremendous efforts have been devoted to the design and exploration of new 2D nanomaterials, which has ultimately led to the identification of a variety of other ultrathin nanomaterials exhibiting an assortment of remarkable chemical and physical characteristics.[2–7] In particular, the phosphorene category reached this class of 2D materials upon the successful isolation

N. Khossossi, D. Singh, W. Luo, R. Ahuja
Condensed Matter Theory Group
Materials Theory Division
Department of Physics and Astronomy
Uppsala University
Box 516, 75120 Uppsala, Sweden
E-mail: rajeev.ahuja@physics.uu.se

R. Ahuja
Department of Physics
Indian Institute of Technology Ropar
Rupnagar, Punjab 140001, India

The ORCID identification number(s) for the author(s) of this article can be found under https://doi.org/10.1002/ente.202200400.

of the ultrathin black phosphorene monolayer (α-P),[8–10] which was found to be a semiconductor exhibiting a direct electronic bandgap of about 1.5 eV along with strongly anisotropic electron and hole mobilities.[8,11–13] Considering the wide scope of available phosphorus allotropes as 3D bulk materials, plenty of other potential 2D material counterparts were suggested. Notably, blue phosphorene (β-P) monolayer was initially predicted computationally and subsequently synthesized successfully through molecular-beam-epitaxy over a gold substrate,[14,15] thereby providing evidence that metastable 2D phosphorus allotropes with outstanding physical properties can be achieved. Following the computational perspective, many other allotropes have been extensively suggested over the past few years, and can differ from each other mostly based on the morphology of their intrinsic puckered structure.[16–24]

As part of the ongoing efforts toward the computational prediction of the 2D holey phase of 2d materials including graphene,[25] phosphorene,[26–28] and transition metal dichalcogenides[29,30] with very outstanding physical properties. Wang et al.[31] recently reported a successful design of the hole-type phosphorene structure through density-functional calculations. They have revealed that the 2D HP system may be employed as a promising membrane for hydrogen purification from different gas mixtures with high selectivity along with being a promising candidate for a solar cell. With this as an underlying motivation, the present paper considers this newly predicted 2D HP monolayer for the electronic, optical, and structural thermoelectric properties. Initially, we survey the structural, environmental stability, and electronic characteristics of the 2D HP nanosheet. To this end, we carry out density functional theory (DFT)-based computations to confirm its dynamical, thermal, and mechanical stability and to address the electronic properties by means of generalized gradient approximation (GGA)- Perdew-Burke-Ernzerhof (PBE), Heyd–Scuseria–Ernzerhof (HSE06), and GW functionals. Furthermore, we also investigated the $G_0W_0 + BSE$ method for the excitonic optical properties, given that no previous related studies have been carried out on this HP with $G_0W_0 + BSE$, which makes the present work an expedient one. The $GW + BSE$ approximation has significantly higher accuracy for the optical properties of excitonic effects owing to its quasi-particle-based characterization. It is obtained that the HP monolayer presents a strong optical adsorption spectrum with three different peaks appearing in the visible-light

zone. Additionally, for the thermoelectric properties, we have consistently calculated the group velocity, the thermal transport properties, and the electrical transport properties based on the entire iterative process of solving the Boltzmann transport equation for phonons. The achieved outcomes reveal favorable results in the electronic bandgap, elastic modulus, optical absorption, phonon group velocity, phonon lifetime, lattice thermal conductivity, and exciton binding energy (EBE) in the 2D HP nanosheet compared to other 2D phosphorene allotropes. The work provided a full perspective into the stability and pivotal physical features of the 2D Holey phosphorus monolayer as well as showcasing its potential to be used for developing next-generation technologies in optoelectronic and thermoelectrical systems.

2. Computational Details

During the present work, the first-principles calculations within the plane-wave basis projector augmented wave (PAW) were employed in the framework of DFT.[32] For the exchange-correlation potential, the GGA in the form of PBE was employed as implemented in the Vienna Ab Initio Simulation Package (VASP) software.[33] The inherent underestimation of the bandgap given by DFT within the inclusion of hybrid functional is corrected by using the HSE06[34] screened-nonlocal-exchange functional of the generalized Kohn-Sham scheme. The charge transfers in the structures were determined by the Bader analysis.[35] The energy cutoff value for the plane-wave basis set was taken to be 500 eV. The total energy was minimized until the energy variation in successive steps became less than 10^{-6} eV in the structural relaxation and the convergence criterion for the Hellmann–Feynman forces was taken to be 10^{-3} eV Å^{-1}. For accurate results, $2 \times 4 \times 1$ Γ centered k-point sampling is used for the primitive unit cell based on the convergence of total energy with respect to different K-points. The Gaussian broadening for the density of states calculation was taken to be 0.10.

The dielectric function and the optical oscillator strength of the HP monolayer were calculated by solving the Bethe–Salpeter equation (BSE) on top of single-shot G_0W_0 calculation, which was performed over standard DFT calculations.[36,37] The G_0W_0 + BSE approach accounts for both e–e and e–h effects. Here, e–e and e–h represent the electron–electron and electron–hole correlation effects, respectively. During this process, we used $2 \times 4 \times 1$ Γ centered k-point sampling. The cutoff for the response function was set to 250 eV. The number of bands used in our calculations is 340. The cutoff energy for the plane waves was chosen to be 400 eV. We included 36 valence (occupied orbitals) and 72 conduction (unoccupied orbitals) bands into the calculations for the dielectric function of HP monolayers in the BSE calculations. In previous investigations, 96 converged empty states for MoS2 monolayer[38] and 150 empty states were taken for GW calculations for the bulk system with semiconductors and insulators by Shishkin and coworkers.[39]

Further, the electron transport properties are computed by using semi-classical Boltzmann transport theory with the relaxation time approximation and rigid band approximation as implemented in the BoltzTraP code.[40] In the thermoelectric properties, we obtain the Seebeck coefficient (thermopower) α

which is independent of the relaxation time τ, electrical conductivity σ, electronic thermal conductivity κ_e which depends on the relaxation time τ. To evaluate the thermoelectric properties, we use the figure of merit, $ZT = S^2\sigma T/\kappa$.

In addition, for the lattice part of thermal conductivity calculations, the Boltzmann transport equation for phonons as employed in the ShengBTE code[41] was adopted. The Phonopy code[42] with $3 \times 3 \times 1$ supercell and $3 \times 3 \times 1$ k-mesh for the second-order force constants were determined. Moreover, third-order force constants were achieved via the finite displacement scheme[43] by displacing two atoms up to seven nearest neighbors (i.e., deviation is $\approx 2.5\%$ observed when six nearest neighbor displacement is considered), consequent to an interaction range of 6.07 Å. We used a q-mesh $28 \times 28 \times 1$ to generate well-converged lattice thermal conductivities. There is no relevant effect in our calculations by taking a very dense q-mesh $32 \times 32 \times 1$.

3. Results and Discussion

3.1. Structural and Electronic Properties

The rectangular unit-cell of the holey-phosphorene (HP) monolayer has been taken in the present work. The fully optimized structure with top and two other orientations of HP monolayer are presented in **Figure 1**a. The unit-cell (marked with a red dashed line) of the HP monolayer contains 10 phosphorus atoms. The top view and side view of the rectangular HP are presented in Figure 1a. The optimized lattice parameters $a = 6.14$ and $b = 7.78$ Å. The P–P bond length is found to be 2.27 Å and the thickness is found to be 2.23 Å, which is good consistent with previously reported work.[31] Alternatively, the structural stability of this new allotrope of phosphorene is roughly assessed with the so-called octet-rule applied to certain non-planar based monolayers, i.e., the P-atom hybridizes in sp^3 and is connected to another 3P-atoms, thus providing 8-electrons within the sp-shell.

Furthermore, to check the HP monolayer stability, we have explored the phonon dispersion spectra by means of the density functional perturbation theory (DFPT) approach and first-principles molecular dynamics (FPMD) simulations. Figure 1b,c shows the phonon band structure along high symmetry points in the Brillouin zine, and FPMD at constant temperature and volume (NVT) of 2D HP nanosheet, respectively. Also, it can be vividly seen the structural rigidity of the monolayer through the phonon band structure. The 2D HP nanosheet shows good dynamical stability since each mode i.e., optical/acoustical branches of phonon dispersion spectrum is positive with linear behaviors around Γ as depicted in Figure 1b. Additionally, the FPMD simulation is carried out at three distinct temperatures 300, 500, and 1000 K as illustrated in Figure 1c, the right side displayed the fully optimized structures at the ends of molecular dynamics simulations at considered temperatures. It can be noticed the slight energy variation as a function of the molecular dynamic simulation time up to 10 ps without any structural distortion and bands breaking between phosphorus atoms. the aforementioned outcomes reveal the high dynamical and thermal stability of the 2D HP nanosheet.
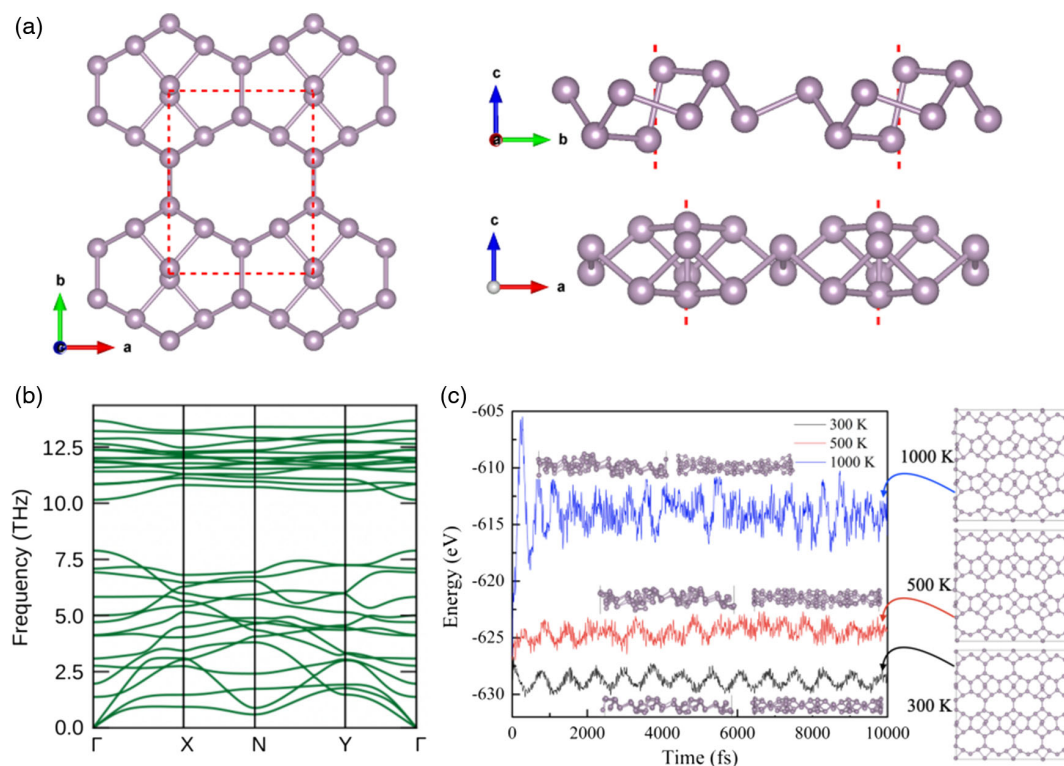
**ADVANCED
SCIENCE NEWS**

www.advancedsciencenews.com

Energy Technology
Generation, Conversion, Storage, Distribution

www.entechnol.de

Figure 1. a) Fully relaxed structure of HP monolayer with top view and side view, b) phonon dispersion profile of holey-phosphorene (HP), c) ab-initio molecular dynamics simulations at different temperatures (300, 500, and 1000 K) for 10 ps. The inserted structure screenshots represent the end of the molecular dynamics steps of the HP monolayer.

Next, we have calculated the elastic constants to verify the mechanical stability of 2D HP nanosheet. The computed elastic stiffness constants C_{11}, C_{12}, C_{22}, C_{66} are found to be 74.89, 21.41, 75.14, and 10.27 N m^{-1}, which satisfy the necessary mechanical equilibrium requirements[44] of Born–Huang (BH) elastic criteria for mechanical stability: $C_{11}C_{22}-C_{12}^2 > 0$ and C_{11}, C_{22}, $C_{66} > 0$. It is quite clear that the HP 2D nanosheet meets all the requirements for mechanical stability. This implies that the material under consideration has high mechanical stability.

Further, we have explored the electronic behavior of HP monolayer through the calculation of the orbital contributed electronic band structure with the corresponding orbital projected density of states as illustrated in **Figure 2**a. It is found that the 2D HP nanosheet presents a semiconductor behavior with an indirect electronic band gap of about 0.78 eV based on the GGA-PBE functional. We further included the spin–orbit coupling (SOC) effect, and subsequently found exactly the same electronic character in the band structure with a band gap of 0.78 eV, indicating that there is no SOC effect on the considered material. Given that GGE-PBE underestimates the electronic bandgap, by including the hybrid-functional HSE06 and GW approach, we achieved a more accurate bandgap. We have found it to be about 1.51 eV using HSE06, while it is about 2.39 eV under the GW approach. As can be seen in Figure 2a, the top of the valence band (VB) is mainly dominated by p-states of P-atoms, whereas the bottom of the conduction band (CB) is strongly hybridized by s- and p-states of P-atoms. Moreover,

the projected density of states reveals that the pz-orbital has a leading contribution in the VB near the Fermi level as in the electronic band structure. It was further identified that the conduction band has a great contribution from the px-orbital with a slight contribution from the other orbitals. Figure 2b depicts the charge density at both the VB maximum and the conduction band minimum.

It is widely recognized that carrier mobility plays a vital role in both electronic and optoelectronic engineering since elevated mobility prevents electrons and holes from re-combining. Consequently, we have derived the effective mass and mobility of electron and hole carriers for the HP nanosheet. The computed effective masses of the electrons (m_e^*/m_0) and holes (m_h^*/m_0) for both CBM and VBM is given by the formula

$$m^* = \hbar^2 \left[\frac{\partial^2 E(k)}{\partial K^2} \right]^{-1} \tag{1}$$

where $\hbar$ and k denote the plank's constant and wave-vector and $E(k)$ shows the respective energy dispersion in CBM/VBM. Thus, the estimated results based on this equation are listed in **Table 1**. One can remark that the effective masses of the electrons along the x/y-directions were somewhat similar, reaching values of about 0.449/0.487 m_0, whereas the effective mass of the holes along the x-direction was roughly 4.8 times greater than that along the y-direction. In this context, it can be concluded that the effective mass of electrons and holes in the 2D HP nanosheet
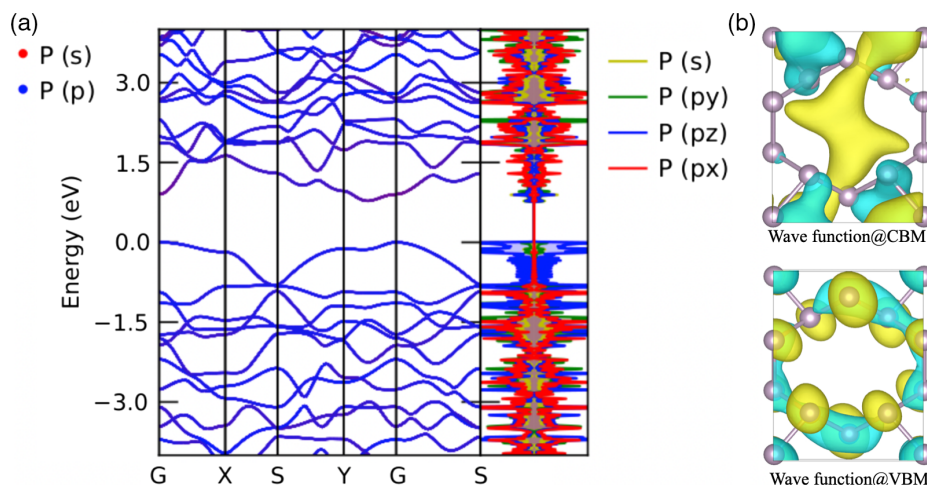
Figure 2. a) The spin-polarized electronic band structure (green and red circles represent the top of the valence band (VB) and bottom of the conduction band (CB) and their difference shown electronic band gap), with corresponding squared wave functions of the bottom of the CB and top of the VB (represented by red and green circle in the band structure). b) Total and projected density of states of HP monolayer.

Table 1. Calculated electron and hole mobility ($\times 10^4$ cm^2 V^{-1} s^{-1}) in the HP monolayer at room temperature along x- and y-direction. m_e^* and m_h^* are the effective masses of electron (e) and hole (h), respectively, deformation potential E (eV) and in-plane stiffness constant C (N m^{-1}), relaxation time constant for electrons/holes along x-/y-directions with the unit of ps.

	m_{ex}^* (m_0)/	m_{ey}^* (m_0)/	E_{1x}	E_{1y}	C_x	C_y	μ_x	μ_y	τ_x	τ_y
e	0.449	0.487	0.74	4.45	74.89	75.14	0.62	0.036	1.58	0.099
h	2.914	0.606	0.12	0.16	74.89	75.14	2.88	7.49	47.70	25.80

was quite similar or slightly lower compared to those of the certain previously reported 2D materials.[45–54] Owing to such low effective masses in the 2D HP nanosheet, it may serve as the leading candidate for high-velocity nanoelectronics applications.

In addition, as a further understanding of the electronic conductance, the carrier mobility was computed utilizing the deformation-potential theory (DPT).[55] The carrier mobility of the HP monolayer has been further calculated according to the given equation

$$\mu_{2D} = \frac{2e\hbar^3 C}{2K_B T |m_*|^2 (E_1^x)^2} \tag{2}$$

where, e and C denote the elementary charge and the elastic-modulus computed through the quadratic fitting of the energy and strain calculations, K_B and m_* are the Boltzmann constant, and the estimated effective mass based on formula 1. E_1^x denotes the DP of the valence band for hole along the x-direction and can be defined as $E_1^x = \Delta E/(\Delta l_x/l_{x,0})$, where ΔE refers to the energy shift in the valence-band as a function of the lattice-parameter change ($\Delta l_x/l_{x,0}$). Meanwhile, the E factor corresponds to the elastic modulus in the x/y-direction. One can vividly notice that the HP monolayer shows a higher electrical-transport bias, and that the electron mobility is superior to that of the holes. Namely, the electron mobility in the x-direction is found to be larger than $0.62/0.036 \times 10^4$ cm^2 V^{-1} s^{-1}. Meanwhile, the hole features a comparatively higher mobility of about $2.88/7.49 \times$

10^4 cm^2 V^{-1} s^{-1} in the x/y-direction. Likewise, strongly an-isotropic carrier mobility values of $0.91/0.88 \times 10^3$ cm^2 V^{-1} s^{-1} along the x/y-directions (electrons) and about $0.18/3.39 \times 10^3$ cm^2 V^{-1} s^{-1} along the x/y-directions (holes) have been consistently reported in the case of single-layered phosphorene material.[56] As a result, the elevated carrier mobility occurs as a consequence of smaller values of both the strain-deformation and the effective mass in the case of the 2D HP nanosheet.

3.2. Excitonic Effect in Optical Properties

It has commonly been revealed that excitonic effects feature prominently in 2D nanomaterials as a result of the near-zero dielectric strength in such materials.[38,57] In line with this, excitonic effects play a crucial role with respect to the optical characteristics and regulate the performance of optoelectronic-based devices that are developed from 2D nanosheets. Taking into account the Coulomb forces of both electrons/ holes is highly relevant while investigating the optical properties of 2D nanosheets. Within this section, we report the findings of our survey on the optical properties of 2D HP nanosheet through solving the BSE equation along with the G$_0$W$_0$ derivation. The EBE for an HP monolayer is obtained to be 1.47 eV along the x-direction and 1.96 eV along the y-direction which is higher compared to some other 2D materials, such as black phosphorene (780 meV),[58] HP nanosheet (80 meV),[59] single layer of graphene (270 meV) and 2D MoS$_2$ (0.96 eV).[38] The imaginary part

**ADVANCED
SCIENCE NEWS**
www.advancedsciencenews.com

Energy Technology
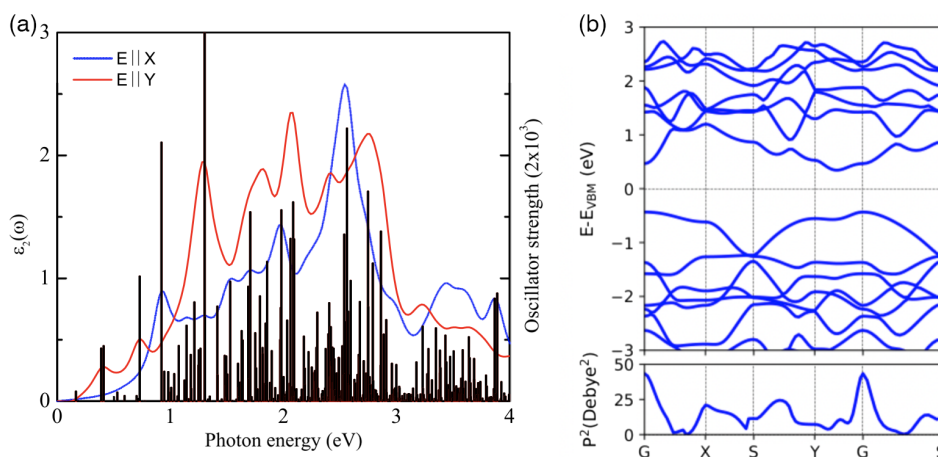Generation, Conversion, Storage, Distribution
www.entechnol.de

Figure 3. a) Imaginary part of the dielectric function of HP monolayer on the left side of the y-axis and oscillator strength of the optical transitions represented by red spike on the right side of the y-axis. b) Corresponding transition probability (p^2) of the electronic band structures for HP monolayer.

of the macroscopic dielectric function (left side of the y-axis), which relates to the absorption spectra and the respective oscillation strength of the optical transitions (right side of the y-axis) are illustrated in **Figure 3**a. As one can clearly notice, there are many excitonic states with very strong oscillation strength. All the three peaks of the absorption spectra appear in the visible region and the first peak appears approximately at 0.92/0.43 eV for x/y-direction, mainly originated from the optical transitions at the high symmetry Γ point in the Brillouin zone as it can be also noticed by maximum transition probabilities at Γ-point depicted in Figure 3b.

Additionally, the real part of the microscopic dielectric function depicts the dispersion and polarization of electromagnetic waves. The static values of the real part of the complex dielectric function at $\omega = 0$ depicted in 4(a) are ≈1.91. Based on the high dielectric constant, significant amounts of charge can be retained for a long time, which may enhance the harvesting of light. As depicted in the figure, the highest peaks of the real dielectric constant for HP monolayer are lactated mainly in the visible-light region between 1 and 3 eV. Consequently, the maximum polarization appeared inside the material. In addition, the reflectivity of the HP monolayer is investigated and illustrated in **Figure 4**d. It can be clearly seen that the HP monolayer shows an ultra-low reflectivity in the whole light-spectrum. the reflectivity spectrum reveals that the maximum value of the reflectivity falls within the visible/UV region (around 3 eV) with a very low value of about 10%. Nevertheless, the reflectivity does not exceed more than 5% in the remaining part of the region. Such findings demonstrate the strong light absorption of HP monolayer. In this regard, the extinction and absorption coefficients confirm the high absorption coefficients confirm the high absorption of light inside the material as illustrated in Figure 4b,c.

3.3. Thermoelectric Properties

3.3.1. Group Velocity and Thermal Transport properties

The lattice thermal conductivity is strongly influenced by group velocities of the material,[60] which is investigated from the slope

of the phonon dispersion and is defined as

$$v_g = \Delta_k \omega(k) \tag{3}$$

where v_g, ω, k and $\omega(k)$ shows the group velocity, angular frequency of wave's, distance between two points in the Brillouin zone and dispersion relation. For lower lattice thermal conductivity, frequency and group velocity should be lower. **Figure 5** shows the group velocities of the 2D HP monolayer. It was seen that the group velocities of acoustical velocities are ≈7 times larger than optical branches. The group velocities of acoustical branches are in the range of 4–7.5 km s^{-1} while for optical branches are 1.1 km s^{-1}. Figure 5b displayed the lattice thermal conductivity (κ_l) which originates from anharmonic phonon–phonon interactions. The (κ_l) decreases with increasing temperature which can be associated with the softening of phonons as temperature increases. The 2D HP monolayer has ultra low (κ_l) because it has more scattering channels. The (κ_l) is found to be ≈0.4 W mK^{-1} at room temperature which is significantly lower than other phases of the 2D phosphorene monolayer.[18,61–65]

In addition, we have calculated the cumulative thermal conductivity κ_{cl} as a function of phonon mean free path (MFP) at room temperature of the 2D HP monolayer (see Figure 5c). The MFP profile is helpful to understand the effect of size on the diffusive phonon transport. This quantity is the ratio of lattice thermal conductivity to lattice thermal conductivity per unit of MFP in a small grain limit grain boundary, which is an approximation of the characteristic size below which nanostructuring induced phonon scattering dominates over anharmonic phonon–phonon scattering.[63] It is a critical for thermal design with nanostructuring as the lattice thermal conductivity could be effectively tuned by nanostructuring when the size of the nanostructure is below the characteristic size. The calculated value is 1.84 nm for the 2D HP monolayer.

3.3.2. Electrical Transport properties

The thermoelectric performance is defined by ZT, which is defined as[66]

ADVANCED
SCIENCE NEWS
www.advancedsciencenews.com

Energy Technology
Generation, Conversion, Storage, Distribution
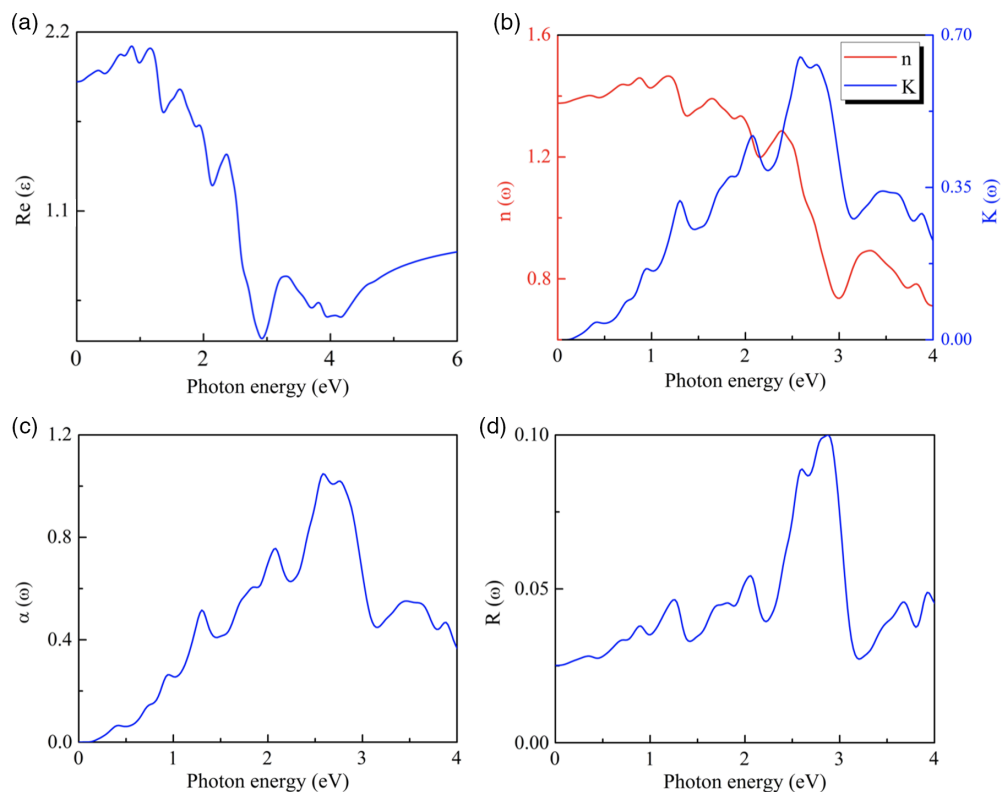www.entechnol.de

Figure 4. Optical properties of HP monolayer. a) Real part of the dielectric function, b) refractive index and extinction coefficient on different γ-axis represented by different colors, c) absorption coefficient, and d) reflectively of HP monolayer.
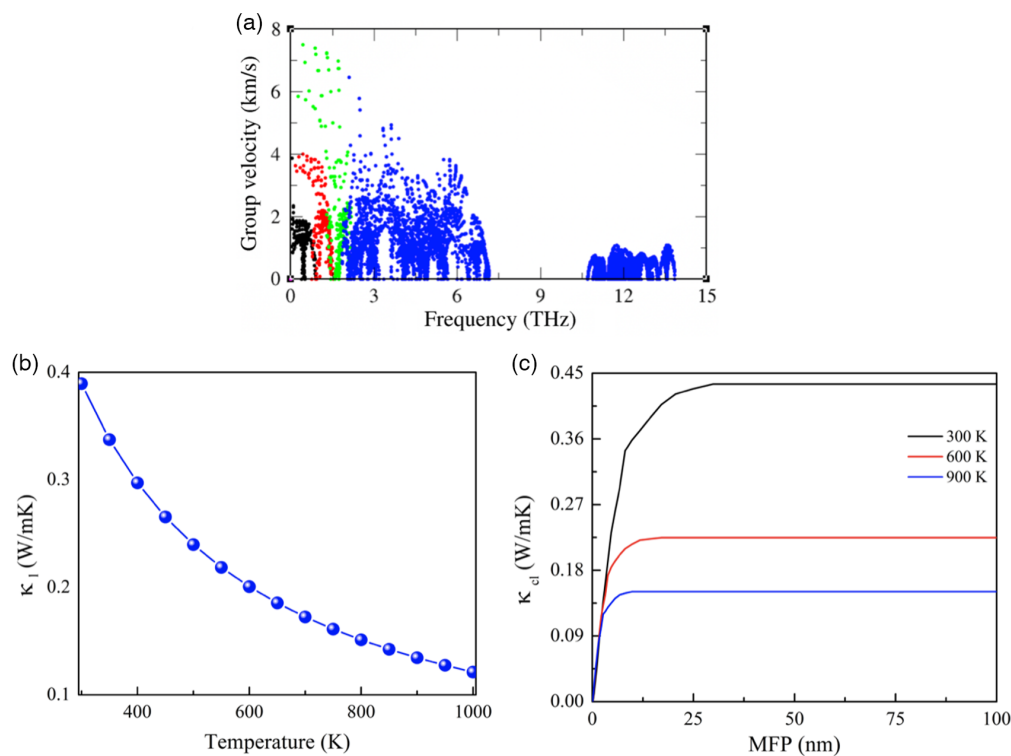

Figure 5. a) Lattice thermal conductivity and b) cumulative lattice thermal conductivity as a function of temperature and mean-free path.

$$ZT = \frac{\sigma S^2 T}{\kappa} \tag{4}$$

where σ, S, T represent the electrical conductivity, Seebeck coefficient, and temperature, respectively, κ shows the sum of electronic thermal conductivity (κ_e) and lattice thermal conductivity (κ_l), i.e., $\kappa = \kappa_e + \kappa_l$. Here, we have calculated the Seebeck coefficient (S), electrical conductivity (σ), electronic thermal conductivity (κ_e), and ZT as a function of chemical potential (μ) as well as temperature.

The effect of doping on the thermoelectric transport coefficient can be obtained by shifting the E_F position. The shift of E_F toward the valence band (i.e., negative E_F) denoted p-type doping, resulting in a positive Seebeck coefficient. Similarly, when E_F shifted toward the CB (i.e., n-type doping can be obtained by negative doping levels) from which we obtained a negative Seebeck coefficient. The electrical transport properties have been calculated by solving semi-classic BTE using a constant relaxation time approximation (CRTA).[67] **Figure 6** shows the S, σ, κ_e and ZT as a function of chemical potential (μ) at different temperatures of 300, 600, and 900 K for a 2D HP monolayer. It was seen that the variation of Seebeck coefficient S is symmetric on both sides for p-type/n-type carriers. The values of S are slightly higher in n-type carriers as compared to the p-type carriers at 300 K. From Figure 6a, the values of S are found to be $1150\,\mu\mathrm{V\,K^{-1}}$ for p-type carriers while $1260\,\mu\mathrm{V\,K^{-1}}$ for n-type carriers. When temperature increases then the values of S are significantly suppressed due to the S is inversely proportional to the temperature. Near the charge neutrality point at particular μ values, S becomes higher and its magnitude shows initially increasing after that decreasing and it was clearly seen that at other temperatures its values are almost the same as 300 K. The electrical conductivity σ as a function of chemical potential μ shown in Figure 6b. The values of σ slightly increase with increasing temperature. The maximum value of σ is found to be $\approx 2\times 10^{19}\,\Omega^{-1}\,\mathrm{m^{-1}\,s^{-1}}$ for p-type carriers whereas $\approx 3.6\times 10^{19}\,\Omega^{-1}\,\mathrm{m^{-1}\,s^{-1}}$ for n-type carriers.

Further, we will discuss the electronic thermal conductivity (kappa_e) for 2D HP monolayer as shown in Figure 6c. The electronic thermal conductivity is directly proportional to electrical conductivity using the Wiedemann–Franz law[68] ($\kappa_e = \sigma LT$, where T is the temperature and L is the Lorentz number). It was seen that the electronic thermal conductivity behaves in a similar trend to electrical conductivity (see Figure 6c). The electronic thermal conductivity for n-type carriers is larger than the p-type carriers at each considered temperature of 300, 600, and 900 K.

It is known that the large value of the ZT displayed superior thermoelectric performance for thermoelectric applications.
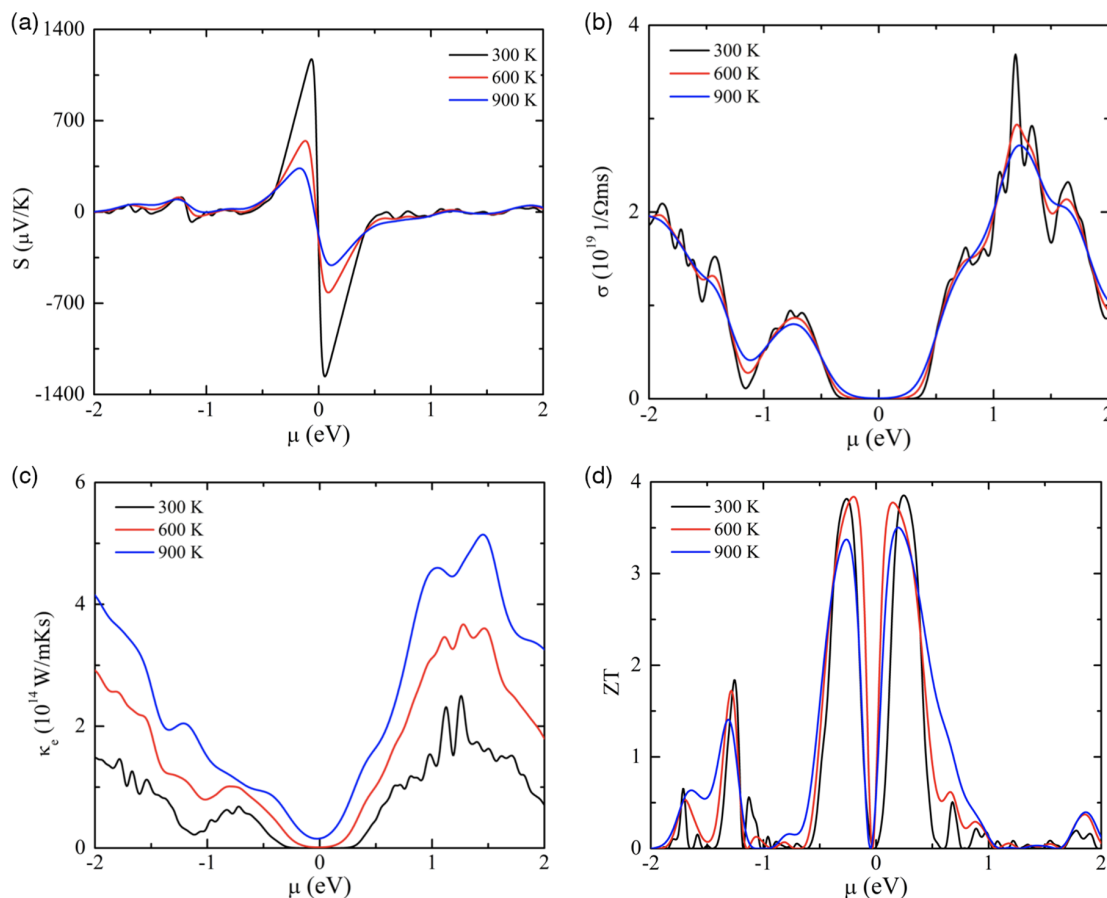

Figure 6. The variation thermoelectric properties of HP monolayer as chemical potential. a) Seebeck coefficient, b) electrical conductivity, c) electronic thermal conductivity, and d) figure of merit (ZT) at different temperatures.

ADVANCED
SCIENCE NEWS
www.advancedsciencenews.com

Energy Technology
Generation, Conversion, Storage, Distribution
www.entechnol.de

Therefore, we have investigated the ZT as a function of chemical potential at three different temperatures for the 2D HP monolayer. It has two strong peaks at the considered temperature in which one peak appears at chemical potential $\mu < 0$ and other peaks at $\mu > 0$ corresponds to the p-type and n-type carriers for ZT values, respectively. It is clearly seen that the ZT values are zero between the two identical peaks. The values of ZT are found to be 3.78 and 3.85 for p-type and n-type carriers at room temperature. Also at a higher temperature, the values of ZT are not significantly affected and its values are above to 3.5 in a 2D HP monolayer. In the present work, the values of ZT are relatively higher than previously reported 2d monolayered materials.[66,69–78]

Finally, we have investigated the thermoelectric conversion efficiency (TCE) of a 2D HP monolayer to see the thermoelectric performance of the considered material which is the main parameter for thermoelectric devices. The TCE for 2D HP monolayer is calculated by the following equation

$$\eta_{max} = \frac{T_h - T_c}{T_h} \frac{\sqrt{1 + (ZT)_{average}} - 1}{\sqrt{1 + (ZT)_{average}} + \frac{T_c}{T_h}} \tag{5}$$

where T_c is the cold side temperature and T_h represents the hot side temperature. Here, we have considered the temperature of 300 K for the cold side leg and 600 K for the hot side leg to calculate the TCE of thermoelectric devices. From the aforementioned relation, the values of TCE are found to be 21.78% and 21.90% for p-type carriers and n-type carriers with the temperature difference $\Delta T = 300$ K. Also, if we take the higher temperatures of the thermoelectric leg for the cold side and hot side (i.e., 600 and 900 K, respectively) then the TCE values are found to be 13.67% and 13.74% for p-type carriers and n-type carriers, respectively. The TCE of 2D HP monolayer material is significantly higher than the previously reported 2D monolayer materials.[75,79,80] These findings of 2D HP monolayer are superior candidates for high-performance optoelectronic devices and high-efficiency thermoelectric devices.

4. Conclusions

In conclusion, we have systematically explored the geometry, optoelectronic, and thermoelectric properties of a newly predicted 2D HP monolayer by using first-principles computations. 2D HP monolayer shows semiconductor behavior with an indirect electronic band gap and intrinsic anisotropic electron/hole mobilities. To calculate accurately the optical properties, the GW plus BSE methods have been utilized. The moderated excitonic binding energy of 1.47 eV along the x-direction and 1.96 eV along the y-direction and the first peak of the absorption spectrum at 0.92/0.43 eV for x/y-direction in the visible light range plays a crucial role in the optical properties. More importantly, the reflectivity is less than 10%, which is much smaller than that of a graphene nanosheet. Therefore, it is interpreted that a 2D HP monolayer can be implemented as a promising antireflective coating medium. In addition, the high thermal power value along with an evaluated electronic ZT of 3.6, which is much higher compared to many recently reported 2D materials, and this

can be explained based on the quantum confinement effect of the nonporous geometry of 2D HP nanosheet. Based on our findings, we believe that the studied 2D HP has excellent physical properties and that this new allotrope of phosphorene could be useful in optoelectronic and thermoelectric engineering technologies.

Conflict of Interest

The authors declare no conflict of interest.

Data Availability Statement

The data that support the findings of this study are available from the corresponding author upon reasonable request.

[1] J. Y. Huang, F. Ding, B. I. Yakobson, P. Lu, L. Qi, J. Li, *Proc. Natl. Acad. Sci.* **2009**, *106*, 10103.

[2] B. Luo, G. Liu, L. Wang, *Nanoscale* **2016**, *8*, 6904.

[3] G. Fiori, F. Bonaccorso, G. Iannaccone, T. Palacios, D. Neumaier, A. Seabaugh, S. K. Banerjee, L. Colombo, *Nat. Nanotechnol.* **2014**, *9*, 768.

[4] N. Khossossi, D. Singh, A. Ainane, R. Ahuja, *Chem. Asian J.* **2020**, *15*, 3390.

[5] K. Novoselov, A. Mishchenko, A. Carvalho, A. Castro Neto, *Science* **2016**, *353*, aac9439.

[6] H. Zhang, *ACS Nano* **2015**, *9*, 9451.

[7] B. Anasori, M. R. Lukatskaya, Y. Gogotsi, *Nat. Rev. Mater.* **2017**, *2*, 1.

[8] J. Qiao, X. Kong, Z. X. Hu, F. Yang, W. Ji, *Nat. Commun.* **2014**, *5*, 1.

[9] M. Köpf, N. Eckstein, D. Pfister, C. Grotz, I. Krüger, M. Greiwe, T. Hansen, H. Kohlmann, T. Nilges, *J. Cryst. Growth* **2014**, *405*, 6.

[10] A. H. Woomer, T. W. Farnsworth, J. Hu, R. A. Wells, C. L. Donley, S. C. Warren, *ACS Nano* **2015**, *9*, 8869.

[11] H. Liu, A. T. Neal, Z. Zhu, Z. Luo, X. Xu, D. Tománek, P. D. Ye, *ACS Nano* **2014**, *8*, 4033.

[12] J. Pang, A. Bachmatiuk, Y. Yin, B. Trzebicka, L. Zhao, L. Fu, R. G. Mendes, T. Gemming, Z. Liu, M. H. Rummeli, *Adv. Mater.* **2018**, *8*, 1702093.

[13] Z. Liu, Y. Sun, H. Cao, D. Xie, W. Li, J. Wang, A.K. Cheetham, *Nat. Commun.* **2020**, *11*, 1.

[14] Z. Zhu, D. Tománek, *Phys. Rev. Lett.* **2014**, *112*, 176802.

[15] J. L. Zhang, S. Zhao, C. Han, Z. Wang, S. Zhong, S. Sun, R. Guo, X. Zhou, C. D. Gu, K. D. Yuan, Z. Li, W. Chen, *Nano Lett.* **2016**, *16*, 4903.

[16] J. Guan, Z. Zhu, D. Tománek, *Phys. Rev. Lett.* **2014**, *113*, 046804.

[17] M. Wu, H. Fu, L. Zhou, K. Yao, X. C. Zeng, *Nano Lett.* **2015**, *15*, 3557.

[18] J. Zhang, H. Liu, L. Cheng, J. Wei, J. Liang, D. Fan, P. H. Jiang, J. Shi, *Sci. Rep.* **2017**, *7*, 1.

[19] J. Liu, Y. Guo, S. Zhang, Q. Wang, Y. Kawazoe, P. Jena, *J. Phys. Chem. C* **2015**, *119*, 24674.

[20] P. G. Demingos, A. R. Muniz, *J. Phys. Chem. C* **2020**, *124*, 21207.

[21] M. Xu, C. He, C. Zhang, C. Tang, J. Zhong, *Phys. Status Solidi RRL* **2016**, *10*, 563.

[22] W. Geng, J. Xiao, J. J. Brown, A. J. Page, Z. Ke, *J. Phys. Chem. C* **2019**, *123*, 10788.

[23] T. Zhao, C. Y. He, S. Y. Ma, K. W. Zhang, X. Y. Peng, G. F. Xie, J. X. Zhong, *J. Phys.: Condens. Matter* **2015**, *27*, 265301.

[24] P. Chuentragool, D. Kurandina, V. Gevorgyan, *Angew. Chem., Int. Ed.* **2019**, *58*, 11586.

[25] A. Lokhande, I. Qattan, C. D. Lokhande, S. P. Patole, *J. Mater. Chem. A* **2020**, *8*, 918.

[26] H. Liu, P. Lian, Q. Zhang, Y. Yang, Y. Mei, *Electrochem. Commun.* **2019**, *98*, 124.

[27] Y. Jiang, X. Li, R. Hou, J. Fu, P. Lian, *Mater. Lett.* **2022**, *317*, 132087.

[28] L. He, Q. Lu, Y. Yang, Y. Liu, Y. Zhu, Y. Mei, *ChemistrySelect* **2021**, *6*, 5021.

[29] Z. Kou, T. Wang, Q. Gu, M. Xiong, L. Zheng, X. Li, Z. Pan, H. Chen, F. Verpoort, A. K. Cheetham, S. Mu, J. Wang, *Adv. Mater.* **2019**, *9*, 1803768.

[30] L. Peng, P. Xiong, L. Ma, Y. Yuan, Y. Zhu, D. Chen, X. Luo, J. Lu, K. Amine, G. Yu, *Nat. Commun.* **2017**, *8*, 1.

[31] H. Wang, X. Li, Z. Liu, J. Yang, *Phys. Chem. Chem. Phys.* **2017**, *19*, 2402.

[32] P. Hohenberg, W. Kohn, *Phys. Rev.* **1964**, *136*, B864.

[33] G. Kresse, J. Furthmüller, *Phys. Rev. B* **1996**, *54*, 11169.

[34] J. Heyd, G. E. Scuseria, M. Ernzerhof, *J. Chem. Phys.* **2003**, *118*, 8207.

[35] G. Henkelman, A. Arnaldsson, H. Jónsson, *Comput. Mater. Sci.* **2006**, *36*, 354.

[36] M. Shishkin, G. Kresse, *Phys. Rev. B* **2006**, *74*, 035101.

[37] F. Karlicky, M. Otyepka, *J. Chem. Theory Comput.* **2013**, *9*, 4155.

[38] D. Y. Qiu, H. Felipe, S. G. Louie, *Phys. Rev. Lett.* **2013**, *111*, 216805.

[39] M. Shishkin, G. Kresse, *Phys. Rev. B* **2007**, *75*, 235102.

[40] G. K. Madsen, D. J. Singh, *Comput. Phys. Commun.* **2006**, *175*, 67.

[41] W. Li, J. Carrete, N. A. Katcho, N. Mingo, *Comput. Phys. Commun.* **2014**, *185*, 1747.

[42] A. Togo, I. Tanaka, *Scr. Mater.* **2015**, *108*, 1.

[43] K. Esfarjani, H. T. Stokes, *Phys. Rev. B* **2008**, *77*, 144112.

[44] F. Mouhat, F. X. Coudert, *Phys. Rev. B* **2014**, *90*, 224104.

[45] Y. L. Lu, S. Dong, J. Li, Y. Wu, L. Wang, H. Zhao, *Phys. Chem. Chem. Phys.* **2020**, *22*, 13713.

[46] C. Wang, X. Liu, Z. Wang, M. Zhao, H. He, Zou J. Electronic, *Chin. Phys. B* **2018**, *27*, 118106.

[47] H. Guo, W. Chu, O. V. Prezhdo, Q. Zheng, J. Zhao, *J. Phys. Chem. Lett.* **2021**, *12*, 3960.

[48] E. Tiras, S. Ardali, T. Tiras, E. Arslan, S. Cakmakyapan, O. Kazar, J. Hassan, E. Janzén, E. Ozbay, *J. Appl. Phys.* **2013**, *113*, 043708.

[49] D. Singh, V. Shukla, P. K. Panda, Y. K. Mishra, H. G. Rubahn, R. Ahuja, *New J. Chem.* **2020**, *44*, 3777.

[50] Z. Y. Ong, G. Zhang, Y. W. Zhang, *J. Appl. Phys.* **2014**, *116*, 214505.

[51] H. Lang, S. Zhang, Z. Liu, *Phys. Rev. B* **2016**, *94*, 235306.

[52] P. Nandi, A. Rawat, R. Ahammed, N. Jena, A. De Sarkar, *Nanoscale* **2021**, *13*, 5460.

[53] Y. Wang, Y. Ding, *J. Phys. Chem. C* **2018**, *122*, 26748.

[54] D. Dimple, N. Jena, A. Rawat, R. Ahammed, M. K. Mohanta, A. De Sarkar, *J. Mater. Chem. A* **2018**, *6*, 24885.

[55] J. Bardeen, W. Shockley, *Phys. Rev.* **1950**, *80*, 72.

[56] G. Schusteritsch, M. Uhrin, C. J. Pickard, *Nano Lett.* **2016**, *16*, 2975.

[57] J. H. Choi, P. Cui, H. Lan, Z. Zhang, *Phys. Rev. Lett.* **2015**, *115*, 066403.

[58] V. Tran, R. Fei, L. Yang, *2D Mater.* **2015**, *2*, 044014.

[59] L. Yang, *Phys. Rev. B* **2011**, *83*, 085405.

[60] D. Singh, R. Ahuja, *Wiley Interdiscip. Rev.: Comput. Mol. Sci.* **2022**, *12*, e1547.

[61] J. Zhang, H. Liu, L. Cheng, J. Wei, J. Liang, D. Fan, et al., *Sci. Rep.* **2014**, *4*, 1.

[62] R. Fei, A. Faghaninia, R. Soklaski, J. A. Yan, C. Lo, L. Yang, *Nano Lett.* **2014**, *14*, 6393.

[63] G. Qin, Q. B. Yan, Z. Qin, S. Y. Yue, M. Hu, G. Su, *Phys. Chem. Chem. Phys.* **2015**, *17*, 4854.

[64] K. Kaur, S. A. Khandy, S. Dhiman, U. Sharopov, J. Singh, *Electron. Struct.* **2022**, *4*, 023001.

[65] S. A. Khandy, *Sci. Rep.* **2021**, *11*, 1.

[66] D. Singh, M. Sajjad, J. A. Larsson, R. Ahuja, *Results Phys.* **2020**, *19*, 103584.

[67] G. K. Madsen, J. Carrete, M. J. Verstraete, *Comput. Phys. Commun.* **2018**, *231*, 140.

[68] T. M. Tritt, *Annu. Rev. Mater. Res.* **2011**, *41*, 433.

[69] F. Q. Wang, S. Zhang, J. Yu, Q. Wang, *Nanoscale* **2015**, *7*, 15962.

[70] L. Medrano Sandonas, D. Teich, R. Gutierrez, T. Lorenz, A. Pecchia, G. Seifert, G. Cuniberti, *J. Phys. Chem. C* **2016**, *120*, 18841.

[71] G. Ding, G. Gao, K. Yao, *Sci. Rep.* **2015**, *5*, 1.

[72] Q. Wang, L. Han, L. Wu, T. Zhang, S. Li, P. Lu, *Nanoscale Res. Lett.* **2019**, *14*, 1.

[73] P. Mishra, D. Singh, Y. Sonvane, R. Ahuja, *Sustainable Energy Fuels* **2020**, *4*, 2363.

[74] D. Singh, S. Kansara, S. K. Gupta, Y. Sonvane, *J. Mater. Sci.* **2018**, *53*, 8314.

[75] D. Singh, N. Khossossi, W. Luo, A. Ainane, R. Ahuja, *Mater. Today Adv.* **2022**, *14*, 100225.

[76] H. Mahida, D. Singh, Y. Sonvane, S. K. Gupta, P. Thakor, R. Ahuja, *New J. Chem.* **2021**, *45*, 3892.

[77] A. Patel, D. Singh, Y. Sonvane, P. Thakor, R. Ahuja, *ACS Appl. Mater. Interfaces* **2020**, *12*, 46212.

[78] D. Singh, R. Ahuja, *ACS Appl. Energy Mater.* **2019**, *2*, 6891.

[79] B. Zhu, X. Liu, Q. Wang, Y. Qiu, Z. Shu, Z. Guo, Y. Tong, J. Cui, M. Gu, J. He, *Energy Environ. Sci.* **2020**, *13*, 2106.

[80] D. Kraemer, J. Sui, K. McEnaney, H. Zhao, Q. Jie, Z. Ren, G. Chen, *Energy Environ. Sci.* **2015**, *8*, 1299.

2200400 (9 of 9)